



# A computer simulation study of the effects of temperature change rate on austenite kinetics in laser hardening



Marko Bojinović<sup>a</sup>, Nikolaj Mole<sup>b</sup>, Boris Štok<sup>b,\*</sup>

<sup>a</sup> TIC–Lens Laser Technologies d.o.o., Celje 3000, Slovenia

<sup>b</sup> Laboratory for Numerical Modelling and Simulation, Faculty of Mechanical Engineering, University of Ljubljana, Ljubljana 1000, Slovenia

## ARTICLE INFO

### Article history:

Received 18 September 2014

Accepted in revised form 31 January 2015

Available online 19 March 2015

### Keywords:

Laser hardening  
Austenitisation kinetics  
Computer simulation  
Phase transformation  
Martensitic transformation  
Hardness measurement

## ABSTRACT

The paper presents a modelling of the laser hardening process by a high-power diode laser (HPDL). Through numerical implementation into the finite element method (FEM) code ABAQUS, the model is used in the computer simulation of two case studies of laser hardening selected for experimental validation. In the experiment,  $100 \times 100 \times 15$  mm cuboid samples made of 50CrV4 steel were subjected to laser hardening with significantly different sets of applied technological parameters (laser beam power, laser beam velocity) but still aiming at attaining a comparable maximum temperature on the sample surface. The simulation considers two alternative approaches to microstructure evolution and subsequent material hardness determination: one relying on the heating rate dependent austenitisation temperatures ( $A_{c1}$  and  $A_{c3}$ ) governing microstructure transformation kinetics and the other neglecting heating rate dependence. Physical objectivity of the computed results is verified based on the corresponding temperature field measurements on the sample surface during heat treatment process and hardness measurements through the thickness of the laser-hardened sample. The experimental validation clearly proves that considering austenite kinetics at a high temperature change rate in computer simulation is definitely more physically congruent. In the study of the applied process parameters impact, the effect of a higher temperature change rate on austenite kinetics is shown by the temperature shift of austenite and ferrite to austenite start formations. From the investigation of the effect of different heat inputs providing the same maximum temperature on the sample surface it results that deeper area of increased hardness is established when less laser beam power and velocity are applied.

© 2015 Elsevier B.V. All rights reserved.

## 1. Introduction

Laser hardening is a heat treatment process that is used to increase hardness of a workpiece surface domain by means of laser beam energy. Aimed at increasing the surface wear resistance, it is mainly used as the final heat treatment that normally transforms microstructure of the heat-affected surface domain while maintaining the microstructure of the interior of the workpiece. Considering the energy field distribution is rather concentrated around the laser beam source, laser hardening is mainly used for local heat treatment of specified workpiece surfaces of various geometrical shapes, such as the surfaces of manufacturing tools that are exposed to sliding, cutting, and/or forming.

The advantages of laser hardening over conventional methods of hardening (e.g., induction hardening, flame hardening, or furnace

hardening) are its flexibility and ability to automate the hardening process and its precise, contactless local heat treatment with no need for additional cooling media such as oil or water. Because the energy of the laser beam heats up the workpiece surface rapidly, a high temperature difference between the heated surface domain and the interior of the workpiece is established. The interior of the workpiece acts as a heat sink because of its significantly larger volume, thus allowing the surface domain to cool quickly after heating and the interior temperature not to increase significantly. This results in a smaller heat-affected zone, less temperature-dependent deformation, and rapid hardening.

Laser hardening enables treatment of different types of steel because there is a wide range of technological parameters available [1]. Directly related to the given laser source are the laser type and its wavelength, nominal power and the power density distribution of the laser beam. The velocity of the laser beam with regard to the workpiece is an additional and significant process parameter [2,3]. For a determination of optimal hardening process parameters, the chemical composition and microstructure of the steel from which the workpiece is made should be known. The microstructure, being dependent on previous mechanical and/or heat treatment performed on the workpiece [4], and the specified heat treatment parameters determine the kinetics of phase

Abbreviations: HPDL, High-power diode laser; FEM, Finite element method; FE, Finite element; TTA, Time–Temperature–Austenitisation diagram; TTT, Time–Temperature–Transformation diagram; CCT, Continuous–cooling–transformation diagram

\* Corresponding author. Tel.: +386 1 4771 427; fax: +386 1 2518 567.

E-mail addresses: [marko.bojinovic@gmail.com](mailto:marko.bojinovic@gmail.com) (M. Bojinović), [nikolaj.mole@fs.uni-lj.si](mailto:nikolaj.mole@fs.uni-lj.si) (N. Mole), [boris.stok@fs.uni-lj.si](mailto:boris.stok@fs.uni-lj.si) (B. Štok).

transformations during the heat treatment process. The amount and type of phase transformation have a key impact on the mechanical state of the workpiece after heat treatment [5].

In order to obtain increased hardness after heat treatment on the surface domain of the workpiece, this domain should be heated above the temperature of austenitisation. In the cooling phase, austenite normally transforms into a mixture of martensite, bainite, pearlite, or ferrite microstructure, depending on the cooling rate of the steel. As the heating rates in laser heat treatment are normally in the order of  $10^2$  to  $10^4$  °C/s, a greater driving force is required to transform the base material to austenite microstructure, which results in a higher austenitisation temperature in comparison to conventional slow heating (e.g., heating in a furnace) [1,2]. The influence of a constant heating rate on the austenitisation temperatures  $Ac_1$  and  $Ac_3$ , the temperature at which austenite begins to form ( $Ac_1$ ) and the temperature at which ferrite completes its transformation into austenite ( $Ac_3$ ), has been experimentally analysed for heating rates up to 2400 °C/s in [6]. It is shown that with an increase in the heating rate, the austenitisation temperatures  $Ac_1$  and  $Ac_3$  increase as well. The dependence of the austenitisation temperatures  $Ac_1$  and  $Ac_3$  at a constant heating rate is well known as the time–temperature–austenitisation (TTA) diagram.

A proper determination of the  $Ac_1$  and  $Ac_3$  temperatures during computer simulation of laser heating is important because of the impact these temperatures have on material properties, kinetics of phase transformation, volume dilatation and latent heat release, amount of transformed microstructure, and a determination of hardness profile. In the literature there are essentially two approaches to the  $Ac_1$  and  $Ac_3$  temperatures determination.

In the first approach, the  $Ac_1$  and  $Ac_3$  temperatures are assumed as heating rate independent. Accordingly, they are constant and equivalent to the  $Ac_1$  and  $Ac_3$  temperatures for conventional slow heating while the phase transformation kinetics during heating is not explicitly defined. The latter is rather simplified and determined by linear interpolation between the austenitisation temperatures [7] or simply defined as on/off function with respect to temperature [8,9]. In [7], the author used linear interpolation of volume dilatation during phase transformation of initial microstructure into austenite, which is in direct correlation to the linear interpolation of microstructural kinetics of considered C15 and C45 steel. The respective austenitisation temperatures were determined in accordance with empirical equations based on chemical composition of the considered steels. Following the on/off approach, the value of the  $Ac_3$  temperature of stainless steel with unspecified composition was determined in [8] to be 780 °C, whereas in [9] the value of 770 °C was presented as the  $Ac_3$  temperature of C60 steel, wherein material has to be heated with a mean temperature of 833 °C for 2 s for complete austenitisation.

Within the second approach, where the austenitisation temperatures are considered as heating rate dependent, there are also different methods for the austenitisation temperatures determination. Among the first to give a comprehensive phenomenology description of the transformation hardening of steel surface by laser beam were Ashby and Easterling [2,3], who developed also corresponding thermal and kinetic model for laser hardening. In their opinion, the pearlite colonies on rapid heating first transform to austenite, then depending on the value of temperature relative to the  $Ac_3$  temperature, a part or all the ferrite may transform too. The pearlite becomes austenite containing 0.8% carbon while the ferrite becomes austenite with negligible carbon content. Thereafter the carbon diffuses from the high to the low concentration regions, to an extent which depends on temperature and time. Considering the above assumptions they presented a pearlite to austenite kinetics law which is governed by interlamellar spacing of the pearlite and thermal history, while the homogenisation of austenite was modelled with carbon diffusion evolution [2]. Based on the developed simple models for pearlite dissolution, austenite homogenization and martensite formation, and considering the resulting temperature

variation  $T(z, t)$ , Ashby and Easterling presented in [2] structural changes caused in hypoeutectoid steels under applied heat cycle. The extent of respective structural change is determined by considering whether the structural change is diffusive or non-diffusive. While the extent of diffusive structural changes depends on the total number of diffusive jumps which take place during the cycle and is measured by the kinetic strength  $I$  of the heat cycle, the extent of non-diffusional structural change, i.e. austenite to martensite transformation, depends on quenching rate  $dT/dt$ , rather than on kinetic strength  $I$ .

After giving a review on the development of kinetics and thermal coupling models that were based on Ashby and Easterling's approach and their further numerical implementation, Skvarenina and Shin presented in [10] a more sophisticated model where coupling of a 2D diffusion model with a 3D transient thermal model was applied in the analysis of laser hardening of a crankshaft made of AISI 1536 steel. By assuming the homogenization of austenite is governed by solute diffusion, Fick's 2nd law of diffusion was used to describe the kinetics. Furthermore, still remaining within Ashby and Easterling's approach, Bailey et al. presented in [11] a full 3D thermal and kinetics model which was then sequentially coupled to a 3D stress model in order to predict residual stresses. They solved the kinetics model by applying explicit finite volume scheme while the homogenisation of austenite was solved with Fick's 2nd law using finite volume method. From [10] it is also evident that the characteristic of all so-called Ashby and Easterling's approach based models is the inconvenience regarding required material properties determination. For proper calculation of microstructural kinetics detailed information of initial microstructure, incorporated diffusion and activation energy has to be either provided experimentally or assumed.

Another heating rate dependent approach for the calculation of austenite kinetics and determination of austenitisation temperatures was proposed by several research groups through a series of publications in [12,13], where the approach was comprehensively introduced and applied to steel XC42. The phase transformation calculation model by heating is based on the additivity rule, where the isothermal transformation kinetics is modelled according to the law developed by Johnson–Mehl [14] and Avrami [15]. The authors in [12] presented the formation of austenite through two steps—first the pearlite dissolution which is followed by the transformation of ferrite. The growth of austenite is modelled by two-phase Johnson–Mehl–Avrami law, one for dissolution of pearlite and the other for the transformation of ferrite, with the beginning of ferrite to austenite transformation being possible after the completed transformation of pearlite to austenite. The authors in [12] used isothermal heating diagram to determine the Avrami exponents used in the calculation of phase transformation during austenitisation. Their first guess of the isothermal heating diagram was estimated from experimental data of continuous heating tests and used to calculate the evolution of transformation during continuous heating, which was then compared to the experimental results. Based on this comparison a new guess of isothermal heating diagram was obtained. By applying the described procedure iteratively the optimal isothermal heating diagram was determined which was then used for further predictions. The authors pointed that the beginning and the end of corresponding transformation kinetics during heating are well predicted and congruent with experimental results most likely because of iterative correction procedure, while especially the calculated amount of pearlite to austenite is subjected to great discrepancy. The disadvantage of this approach is the lack of clarity regarding iterative adapting of isothermal heating diagram and also sensitivity of the calculated thermal field accuracy, which can impact the estimation of isothermal heating diagram.

In [16], still using Avrami approach, Mioković et al. also summed up their research on the effect of heating rate on the formation of austenite microstructure and the effect of cooling rate on the formation of martensite microstructure in case of a short time hardening process. In their first experiment, hollow cylindrical specimens with an outer

diameter of 8 mm and wall thickness of 1 mm were heated up using electrical resistance heating and afterwards cooled inside using a mixture of water and pressurised air. Assuming in the experiment constant heating rates of  $1 \times 10^3$ ,  $3 \times 10^3$ , and  $10 \times 10^3$  °C/s and cooling rates of  $1 \times 10^3$  and  $3 \times 10^3$  °C/s, they found that the microstructure development during a short time austenitisation is affected by heating and cooling rates. In the subsequent experiment a stationary laser was used for heating of cylindrical 6-mm workpieces made of 42CrMo4 steel. Results of this experiment were used to adequately describe the material behaviour, which was then implemented into the finite element (FE) program ABAQUS [17] taking user-defined material laws into account. Based on such a model, a coupled computation of the temperature and microstructure phase transformation evolution during rapid heating and cooling is performed by means of constant heating rate 1000 K/s. As regards the resulting hardness profiles and the degree of homogeneity of the hardened structure, a good accordance between results of the computer simulation and the experiment was obtained. Such high heating and cooling rates, as considered above, are characteristic only of stationary energy input at initial stages of laser heat treatment or heat treatment where laser beams with relatively small diameters are used. With laser heat treatment using a moving high-power diode laser, the presented heating rates are characteristic only of the beginning of laser heat treatment. In general, they are lower and variable throughout the heat treatment process, which has to be taken into account.

In [18], an extended and complex numerical model for the calculation of thermo-mechanical and metallurgical behaviour of 42CrMo4 steel by laser hardening is built by Yaakoubi et al. The experimental case from [11] was numerically simulated, while the austenitisation and diffusive kinetics were determined by using the algorithm of Farias [12]. The authors also predicted transformation temperatures  $A_{c1}$  and  $A_{c3}$  and associated constant heating rates, while the calculation method of heating rates is not revealed.

The third heating rate dependent approach considering austenite kinetics was introduced by Orazi et al. in [19], where a model able to predict the austenitisation of hypo-eutectoid steels during very fast heat cycle such as laser hardening is presented. The main feature of the proposed new austenitisation model, which is based on Ashby and Easterling's pearlite dissolution equation, is the pearlite to austenite transformation time parameter  $I_{p \rightarrow a}$ , by means of which the typical hardness transition from the treated surface to the base material can be estimated. As the  $I_{p \rightarrow a}$  parameter is a function of the temperature variation, it can be considered as a grain property associated with the hardness profile. In this regard, threshold values  $I_{p \rightarrow a, min}$  and  $I_{p \rightarrow a, max}$  are postulated as material physical constants, the value of which is determined by experimental heat cycle tests. For a grain characterised in heat cycle by  $I_{p \rightarrow a} \leq I_{p \rightarrow a, min}$  there is no transformation of pearlite to austenite, whereas for a grain proving  $I_{p \rightarrow a} > I_{p \rightarrow a, max}$  the transformation from pearlite to austenite is completed. By considering  $I_{p \rightarrow a}$  having a linear distribution between  $I_{p \rightarrow a, min}$  and  $I_{p \rightarrow a, max}$ , a continuous distribution of austenite fraction that will generate a continuous distribution of martensite after quenching is obtained for grains proving  $I_{p \rightarrow a, min} < I_{p \rightarrow a} \leq I_{p \rightarrow a, max}$ . By the proposed austenitisation criteria the resulting hardness profile calculation is based on a smooth transition between the start and the end of pearlite to austenite transformation, rather than on on/off behaviour. The described approach proved to be computationally efficient and yielding results that were in good agreement with various experiments on steel AISI 1045. Although the approach is highly innovative and useful for process design of treated steel, the consideration is based on the main assumption that, because of the high heating rate, hardness reduction is mainly due to partial pearlite transformation during heating, while effect of partial carbon diffusion on hardness distribution is neglected.

The fourth heating rate dependent approach for the calculation of austenite kinetics and determination of austenitisation temperatures was introduced by Geijselaers in [20], where a very detailed method

to simulate solid state transformation within laser hardening is presented and demonstrated by a series of 1D and 2D simulations for specific laser hardening cases. Regarding kinetics of phase transformation during heating the author introduced industrially applicable mathematical model that can be incorporated in FEM numerical models. For the calculation of pearlite to austenite and ferrite to austenite kinetics, he suggested Avrami based approach where phase transformation time constant was introduced, while complete procedure of isothermal transformation curves estimation was obtained from continuous transformation data for heating and cooling. The procedure uses time temperature transformation diagram (TTA) for the calculation of transformation kinetics during heating, which makes it, because of a wide range of available TTA diagrams for various steels, highly appropriate for use in industry. The procedure also provides a straight forward calculation of austenitisation temperatures and phase transformation kinetics during heating within short time austenitisation processes.

The most relevant features characterising the process of laser hardening can be briefly summarised as follows. Evolution of the temperature field during laser hardening is determined; the material properties of the workpiece are subjected to heat treatment through imposed heating and cooling conditions. The heating conditions are determined by considering technical characteristics of the used laser source (wavelength, nominal power, power density distribution of the laser beam) and applied process parameters (velocity and direction of the laser beam movement, area exposed to laser heating). The established heating rate is very high at the beginning of laser hardening, due to rapid heating of the initially cold workpiece surface. Later, when the workpiece surface's maximum temperature is reached, gradients of the evolved temperature field are much smaller, whether the laser beam is fixed or moving. Different heating rates established in the heat-affected domain of the workpiece are reflected in different  $A_{c1}$  and  $A_{c3}$  temperatures, which in turn determine the amount of phase transformation and, consequently, development of related strains and stresses.

In this paper, a complex numerical model for laser hardening based on the finite element method (FEM) is introduced with the aim of transferring the above exposed physical complexity of laser hardening to a virtual environment. After adequate experimental validation, such a model can be used in computer simulation of the laser hardening process under realistic industrial conditions. The model thus enables a detailed analysis of the effect of individual process parameters on the obtained microstructure and resulting mechanical properties of the workpiece after laser hardening, considering heating rate-dependent  $A_{c1}$  and  $A_{c3}$  temperatures where the model suggested by Geijselaers [20] was adopted. In this paper, the effect of the initial microstructure and the influence of temperature and its changing rate on the kinetics of the microstructure evolution of 50CrV4 steel is considered in a computer simulation, assuming significantly different technological parameters. The computer simulation results were experimentally validated, achieving good agreement with the experimental temperature and hardness data.

## 2. Mathematical model

For construction of an appropriate mathematical model that would encompass all physical phenomena relevant to the laser heat treatment process characterisation, understanding phase-transformation kinetics and its dependence on temperature and temperature change rate is essential. Such a model should include a proper description of thermal conditions and mechanisms governing the development of the microstructure constituents in the material of the workpiece and the resulting material properties that depend both on temperature and actual microstructure. Accordingly, the corresponding mathematical model is built from two sets of equations governing the temperature and microstructure field distributions and their time evolution in the considered domain of interest. Because of mutual interdependence between the

thermal and microstructure state variables, the considered problem belongs to a class of coupled problems. In this paper, any possible effect of the mechanical state on the kinetics of microstructure formation and/or temperature field evolution is neglected.

### 2.1. Governing equations of the heat transfer problem

The first set of coupled problem equations that defines the heat transfer problem comprises differential equations governing heat conduction in the heat-treated workpiece

$$\rho c_p \frac{\partial T}{\partial t} = \text{div}(\lambda \nabla T) + \dot{Q} \quad (1)$$

and associated initial and boundary conditions. Above,  $T = T(x, y, z, t)$  is a time-dependent temperature field:  $t$  is time and  $\dot{Q} = \dot{Q}(x, y, z, t)$  is the rate of the latent heat absorbed or released during phase transformation per unit volume. For an individual constituent  $k$  with the rate of volume fraction change  $\dot{\varphi}_k$ , the latter is determined considering the respective change of the enthalpy  $\Delta Q_k^L$  as

$$\dot{Q}_k = \Delta Q_k^L \dot{\varphi}_k \quad (2)$$

Further, the quantities  $\rho$ ,  $\lambda$ , and  $c_p$  in Eq. (1) represent respectively the density, thermal conductivity, and specific heat of the workpiece material. As the material is a mixture of different constituents with volume fractions  $\varphi_k$  whose values are changing in accordance with the temperature evolution, the actual values for the material properties  $\rho$ ,  $\lambda$ , and  $c_p$  have to be determined considering the mixture rule (see Eq. (8)).

The initial temperature field in the workpiece is assumed to be uniform and equal to the surrounding temperature  $T_0$ .

$$T(x, y, z, t = 0) = T_0 \quad (3)$$

The boundary conditions for the considered laser hardening being of the Neumann type, the heat flux at all surfaces of the workpiece is specified. In general, the total heat flux  $\lambda \partial T / \partial n$  through the surface is defined by the following equation:

$$\lambda \frac{\partial T}{\partial n} = q - h(T - T_0) - \sigma \varepsilon (T^4 - T_0^4), \quad (4)$$

where individual contributions on the right side are attributed to a given external heat source: convection and radiation. The heat flux  $q$  is not zero on the surface that is exposed to the laser beam; otherwise it is zero. In the cooling phase (after turning off the laser source), the heat flux  $q$  is zero everywhere. The last two terms in Eq. (4) represent respectively the heat loss due to convection and heat loss due to radiation, with  $h$  being the heat transfer coefficient,  $\sigma$  the Stefan–Boltzmann constant, and  $\varepsilon$  the emissivity of the workpiece's surface. The non-zero heat flux distribution  $q$  is determined in accordance with the characteristic of the applied laser and prescribed process parameters, which is described in detail in Section 2.3.

### 2.2. Governing equations of transformation kinetics

The material is a combination of different constituents, such as ferrite ( $\varphi_F$ ), pearlite ( $\varphi_P$ ), austenite ( $\varphi_A$ ), bainite ( $\varphi_B$ ), and martensite ( $\varphi_M$ ), with  $\varphi_k$  representing the volume fraction of an individual constituent and  $\omega_k$  representing the respective mass fraction. In this regard, let  $\Phi$  denote the compound variable  $\Phi = \{\varphi_F, \varphi_P, \varphi_A, \varphi_B, \varphi_M\}$ , which is an additional state variable in the considered problem. The framework for a determination of the microstructure evolution in the considered domain that yields the actual microstructure field  $\Phi(x, y, z, t)$  through

the workpiece at any considered stage of the laser hardening process is given by the second set of the coupled problem equations.

Not all constituents normally exist simultaneously at a given material point of the workpiece but are formed based on the time variation of the temperature. In principle, individual volume and mass fractions  $\varphi_k$  and  $\omega_k$  are confined to  $0 \leq \varphi_k \leq 1$ ,  $0 \leq \omega_k \leq 1$ ;  $k \in \mathcal{P} = \{F, P, A, B, M\}$ , while their sum respects the volume and mass integrity constraint:

$$\sum_{k \in \mathcal{P}} \varphi_k = 1, \quad \sum_{k \in \mathcal{P}} \omega_k = 1. \quad (5)$$

Given the small difference in the densities of individual constituents of the considered material, it can be assumed that the mass fractions of individual constituents are equal to their volume fractions:  $\varphi_k \approx \omega_k$ . Thus, the value of an individual material physical property  $F$  at temperature  $T$  is determined by taking the actual state of the mixture  $\Phi$  into account, which yields

$$F(T, \Phi) = \sum_{k \in \mathcal{P}} \varphi_k F_k(T, \varphi_k), \quad (6)$$

where  $F_k(T, \varphi_k)$  is the value of the physical property appertaining to the constituent  $k$ .

As already noted, not all constituents normally exist simultaneously at a given material point but are formed based on the time variation of the temperature by taking into account the microstructure of the base material, the actual heating and/or cooling rate, and respective austenitisation temperatures  $Ac_1$  and  $Ac_3$ . In the sequel, a description of the phase transformation calculation models is given, for heating and cooling, respectively, which is followed by a description of the material hardness calculation model.

#### 2.2.1. Phase transformation model – heating

At the beginning of the laser hardening process, the base steel material of a specified chemical composition is assumed to be homogeneous through the workpiece, with the volume fractions of pearlite and ferrite determined based on the carbon content. For hypo-eutectoid steels containing less than 0.8 wt.% C, the volume fractions under question are calculated using the lever rule method [1]:

$$\varphi_P = \frac{C_a - C_F}{0.8 - C_F}; \quad \varphi_F = 1 - \varphi_P, \quad (7)$$

where  $C_a$  and  $C_F$  are the concentrations of carbon in the entire microstructure and in ferrite, respectively, with the latter being negligible.

The method used in this paper for calculating phase transformations during continuous heating from isothermal data is based on the rule of additivity proposed by Scheil [21]. The method considers that continuous heating/cooling occurs through a series of isothermal steps, and the time spent at each of these steps depends on the rate of heating/cooling. Incubation for the transformation occurs progressively as the steel heats/cools, and at each isothermal step, the incubation of transformation can be expressed as the ratio of heating/cooling time for the temperature interval to the incubation period. According to Scheil's additivity rule, if  $\tau$  is the isothermal time required to reach a certain amount of transformed constituent, the same transformation amount will be reached in time  $t_{tr}$  under non-isothermal conditions when Scheil's sum ( $S$ ) equals unity [21]:

$$S = \int_0^{t_{tr}} \frac{d\xi}{\tau(\xi)} = 1. \quad (8)$$

As the time of observation  $0 \leq \xi \leq t_{tr}$  considered in the above integral relation corresponds to the interval  $t_{st} \leq t \leq t_{st} + t_{tr}$  in the real time domain, the function  $\tau(\xi)$  depends in fact on the actual temperature

variation  $T(t)$ . Therefore,  $\tau(\xi) = \tau(T(t))$ , and  $\tau(T)$  is calculated, as suggested in [20], as

$$\tau(T) = \frac{dT}{dc}, \quad (9)$$

where  $c$  is the temperature rate ( $c = dT/dt$ ).

When the temperature–time curve  $T(t)$  is discretised into a series of isothermal steps, the volume fraction of a new phase formed in the individual step is calculated by using isothermal transformation kinetics. The isothermal transformation kinetics is modelled according to the law developed by Johnson and Mehl [14] and Avrami [15] and recently modified by Geijselaers [20]. When heating ferrite–pearlite steel, pearlite transforms to austenite first, as temperature increases above  $Ac_1$ . Once pearlite has transformed to austenite, the austenite further grows by consuming the remaining ferrite, either partially, when temperature is between  $Ac_1$  and  $Ac_3$ , or completely, if the temperature is above  $Ac_3$  [22]. In [20], the transformation kinetics from pearlite to austenite is governed by the following rate equation:

$$\dot{\varphi}_p = -\varphi_p \frac{n_p}{\tau_p} \left( \ln \frac{\bar{\varphi}_{p_0}}{\varphi_p} \right)^{(n_p-1)/n_p}, \quad (10)$$

where  $\dot{\varphi}_p$  is the isothermal rate of change of the pearlite volume fraction,  $\varphi_p$  is the volume fraction of pearlite,  $\bar{\varphi}_{p_0}$  is the equilibrium phase content of pearlite at room temperature,  $n_p$  is the Avrami exponent (which depends on the ratio between nucleation rates and growth rates), and  $\tau_p$  is the isothermal time required to reach transformation from pearlite to austenite. As suggested in [20],  $n_p$  is equal to 2.5.

In [20], the author also suggested that until all the pearlite has been transformed into austenite, there is not sufficient carbon available to transform the ferrite into austenite with the required carbon content; furthermore, he suggested that while pearlite is still present, the equilibrium fractions of austenite and ferrite are corrected for the carbon deficiency. The equilibrium phase content of ferrite  $\bar{\varphi}_F$ , corrected for carbon deficiency in austenite is calculated as

$$\bar{\varphi}_F = \bar{\varphi}_F + (\varphi_{F_0} - \bar{\varphi}_F) \frac{\varphi_p}{\bar{\varphi}_{p_0}}, \quad (11)$$

where  $\varphi_{F_0}$  and  $\bar{\varphi}_F$  are, respectively, the initial and equilibrium phase content of ferrite. Accordingly, the isothermal rate of change of the ferrite fraction corrected for carbon deficiency is described by the following rate equation:

$$\dot{\varphi}_F = (\bar{\varphi}_F - \varphi_F) \frac{n_F}{\tau_F} \left( \ln \frac{\bar{\varphi}_{F_s} - \varphi_{F_0}}{\bar{\varphi}_F - \varphi_F} \right)^{(n_F-1)/n_F}. \quad (12)$$

In the above equation,  $\dot{\varphi}_F$  is the isothermal rate of change of the ferrite volume fraction,  $\varphi_F$  is the volume fraction of ferrite, and  $n_F$  is the Avrami exponent. As suggested in [20],  $n_F$  is equal to 1.

Considering the transformation kinetics from pearlite and ferrite to austenite, given respectively by the rate Eqs. (9) and (12), the isothermal rate of change of austenite  $\dot{\varphi}_A$  is determined according to

$$\dot{\varphi}_A = -\dot{\varphi}_p - \dot{\varphi}_F. \quad (13)$$

Transformation of ferrite–pearlite steel into austenite is finished at  $Ac_3$  temperature with austenite content volume assumed to be 100% [22]. It is also important to emphasise that austenite above  $Ac_3$  is not homogeneous in its composition [13]. Namely, when ferrite dissolution is just complete, the austenite has a lower concentration than austenite that was transformed from pearlite. The rate of dissolution of ferrite depends on initial grain size as well as on time and temperature above  $Ac_3$  for specific steel [22].

### 2.2.2. Phase transformation model – cooling

The phase transformation for diffusional transformations during cooling is governed by the same type of differential equation, as encountered during heating (e.g., Eq. (12)). Accordingly, for the constituent  $k$ , the respective rate equation reads

$$\dot{\varphi}_k = (\bar{\varphi}_k - \varphi_k) \frac{n_k}{\tau_k} \left( \ln \frac{\bar{\varphi}_k - \varphi_{k_0}}{\bar{\varphi}_k - \varphi_k} \right)^{(n_k-1)/n_k}, \quad (14)$$

where  $\tau_k(T)$  can be obtained from the TTT diagram or estimated from the CCT diagram, as proposed by Geijselaers in [20].

In this investigation we are focused on the hardness established at the end of cooling while remaining aware that because of characteristic cooling rates in laser hardening and high hardenability of the considered steel, all the austenite transforms to martensite, the respective fraction can be calculated, regardless of the above rate law, by the Koistinen–Marburger equation [11]:

$$\varphi_M(T) = \varphi_A \left( 1 - e^{\beta(T_{Ms} - T)} \right) \text{ for } T < T_{Ms}. \quad (15)$$

The fraction of martensite formed  $\varphi_M(T)$  depends essentially on the volume fraction of austenite  $\varphi_A$  when temperature reaches  $T_{Ms} = 290$  °C, i.e. the temperature by which the martensite structure starts to form from austenite. The coefficient  $\beta = -0.02$  is determined from [23].

### 2.2.3. Material hardness model

The basis for material hardness determination in the laser heat-treated material is the microstructure resulting at the end of the heating phase. The hardness  $H_c$  of the material point can be thus predicted by considering the actual microstructure and the maximum temperature attained at the point during heat treatment. In this regard, the material points can be classified, as proposed in [13], into four distinct temperature areas: T-1, T-2, T-3, and T-4 (each having a specific impact on the hardness).

In the first area, T-1, where maximum temperature is below  $Ac_1$ , the hardness is assumed to be the same as the initial average measured hardness of the base material.

In the second and third areas, T-2 and T-3, with maximum temperature being between  $Ac_1$  and  $Ac_3$ , the hardness is calculated in accordance with Eq. (6), which yields

$$H_c = \sum_k \varphi_k H_k, \quad (16)$$

where  $\varphi_k$  is the fraction of constituent  $k$ , and  $H_k$  is its corresponding hardness. The hardness of martensite in the T-2 and T-3 areas is calculated in HV by

$$H_M = 1667c - 926 \frac{C_a^2}{\varphi_M} + 150, \quad (17)$$

where  $C_a$  is a nominal amount of carbon in the steel and  $\varphi_M$  is a volume fraction of martensite [11]. For the fractions of ferrite and pearlite that do not undergo phase transformation, respective hardness is assumed to be  $H_F = 150$  HV, obtained from [10], and  $H_P = 365$  HV, which is obtained upon hardness measurement of the base material. For a constituent that during heating undergoes phase transformation to austenite and subsequently during cooling transforms to ferrite, pearlite, or bainite, the corresponding hardness  $H_k$  is calculated according to [24]. In the T-2 area, only pearlite is transformed into austenite with high carbon content, whereas in the T-3 area, with all the pearlite transformed, ferrite transforms, partially or fully, into austenite with low carbon content.

For material points belonging to the fourth area, T-4, the austenitisation has reached completion and the homogenisation

of austenite occurs. Considering the microstructure is homogeneous austenite, the peak hardness due to laser heat treatment is higher than the peak hardness established by conventional heat treatment (e.g., in a furnace) in this temperature area. The following equation, proposed in [25], is used for the respective hardness calculation in HV:

$$H_c = 279.69 + 1024.9C_a \tag{18}$$

### 2.3. Laser energy input characterisation

The input of energy into the workpiece, provided in the heating phase of the laser hardening process by the applied laser in the form of heat flux  $q$  distribution (see Eq. (4)), depends primarily on the laser's physical properties: laser beam power  $P$  and laser beam intensity distribution  $I(x, y)$ . For the purpose of adequate mathematical description, it is advantageous to set in the plane of the workpiece surface subject to laser heating a local coordinate system  $(x, y)$  with the origin at the centre of the laser beam intensity distribution. By fixing the local coordinate system to the laser, the system follows any laser displacement by exhibiting related in-plane rigid body motion degrees of freedom.

In general, the following relationship holds between the laser beam power  $P$  and laser beam intensity distribution  $I(x, y)$ :

$$P = \int_{-\infty}^{\infty} \int_{-\infty}^{\infty} I(x, y) dx dy \tag{19}$$

For HPD-type lasers, the laser beam intensity distribution can be described with the super-Gaussian (SG) function [26]. Thus, we have

$$I(x, y) = I_0 \cdot e^{-R(x, y)} \tag{20}$$

with  $I_0 = I(0, 0)$  representing the peak value of the distribution and  $R(x, y)$  determining its shape. The magnitude of the peak intensity can be deduced from Eqs. (19) and (20), which yield the following relationship:

$$I_0 = \frac{P}{\int_{-\infty}^{\infty} \int_{-\infty}^{\infty} e^{-R(x, y)} dx dy} \tag{21}$$

The functional form of the exponent  $R(x, y)$  is given by this equation:

$$R(x, y) = \left| \frac{x}{a} \right|^m + \left| \frac{y}{b} \right|^n \tag{22}$$

where the geometrical parameters  $a$  and  $b$  define the size of the

interaction area of the laser beam with the workpiece, and parameters  $m > 0$  and  $n > 0$  specify the shape of the distribution. As follows from Eqs. (20) and (21), the parameters  $a$  and  $b$  are determined by identifying points  $(|x| = a, |y| = b)$ , where the intensity  $I(x, y)$  drops to the value of  $I_0 \cdot e^{-2}$ . A distribution with the values  $m = n = 2$  is called Gaussian and results in an elliptical laser beam interaction area. When increasing the  $m$  and  $n$  values, the shape of the interaction area becomes more and more rectangular, while the intensity distribution  $I(x, y)$  becomes uniform in this area and vanishes outside. In the limiting case, as the parameters  $m$  and  $n$  tend towards infinity, a uniform distribution of the magnitude  $I(x, y) = I_0$  is established in the interior of the rectangular area  $|x| \leq a, |y| \leq b$ .

For sufficiently large values of the parameters  $m$  and  $n$ , which are actually technical characteristics of the laser used in our investigation [27], the area influenced by the laser beam can be approximated by a rectangle of dimensions  $2a \times 2b$ , and the effect of the laser beam intensity distribution outside this area on the heat flux distribution  $q(x, y)$  can be considered negligible. Taking those properties into account, the following simplified expression for the heat flux distribution  $q(x, y)$  can be applied:

$$q(x, y) = \frac{P \cdot A \cdot e^{-R(x, y)}}{\int_{-a}^a \int_{-b}^b e^{-R(\xi, \eta)} d\xi d\eta} \cong \frac{P \cdot A \cdot e^{-R(x, y)}}{2a \cdot 2b} \tag{23}$$

where  $A$  represents the absorptivity of the workpiece surface.

Time variation of the heat flux distribution  $q(x, y)$  depends on the laser motion. In this regard, let set in the global coordinate system  $(X, Y, Z)$ , whose plane  $(X, Y)$  is coplanar with the plane  $(x, y)$  of the local coordinate system, the starting position of the centre of the laser beam  $(x = y = 0)$  at time  $t = 0$  to the point  $(X_0, Y_0)$ . Assuming that the laser beam motion is planar and translatory, the corresponding time variation of the laser beam centre position  $(X_{LB}(t), Y_{LB}(t))$  is governed by the prescribed velocity vector  $(v_x(t), v_y(t))$ . Thus, we have

$$X_{LB}(t) = X_0 + \int_0^t v_x(\xi) d\xi, Y_{LB}(t) = Y_0 + \int_0^t v_y(\xi) d\xi \tag{24}$$

For a proper transformation of the heat flux distribution  $q(x, y)$ , which is given in the local coordinate system by Eq. (23), the relationship between the global and local coordinate system (see Fig. 1 and Fig. 5) must be respected:

$$x(t) = X - X_{LB}(t), y(t) = Y - Y_{LB}(t) \tag{25}$$

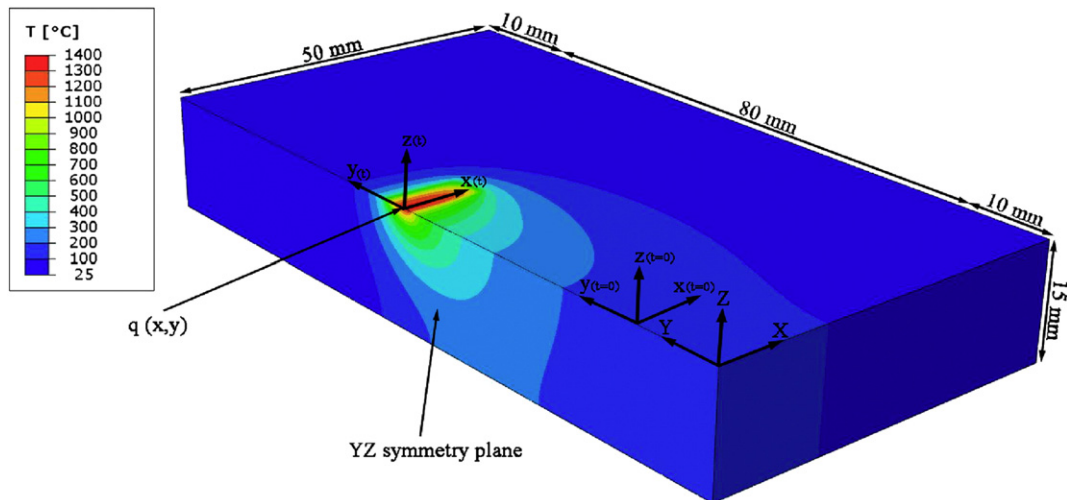


Fig. 1. Temperature field distribution during the laser hardening process.

**Table 1**  
Chemical composition of 50CrV4 steel.

Element	C	Si	Mn	Cr	Mo	Ni	V	P	S
Wt [%]	0.500	0.310	0.930	0.930	0.040	0.150	0.120	0.013	0.005

### 3. Computer simulation

In order to prove physical adequacy of the herein presented numerical approach to the kinetics of phase growth and subsequent hardness field determination by means of a corresponding computer simulation, a numerical model addressing the governing equations of the previous section in a discrete way should be built. With such a model, simulations considering different laser hardening process data and possible physical approaches to the hardness determination can be run and validated. Mainly because of the experimental validation, the simulation studies performed in this investigation are focused on  $100 \times 100 \times 15$  mm cuboid samples made of steel 50CrV4, with two different sets of process parameters applied.

#### 3.1. Numerical model

A 3D numerical model based on the FEM was built in the program ABAQUS. For adequate fulfilment of the considered physical behaviour described in the previous section, its implementation includes a series of user-defined subroutines. By paying attention to adequate refinement in the domains where the evolution of the physical state variables is much more intense, the analysed cuboid domain is discretised by 760,000 8-node FEs (ABAQUS notation – DC3D8). The FE mesh is thus denser in the interaction area of the laser beam with the workpiece, where the highest temperature gradient is manifested, and in the domain of expected phase transformations. The characteristic size of the elements in the refined FE mesh domain is  $0.56 \times 0.13 \times 0.10$  mm.

Because in the real laser hardening experiment the laser is moving along a symmetry line of the workpiece ( $v_x(t) = 0$ ), which is coincident with the global Y-axis (see Fig. 1), symmetrical field distributions with respect to the YZ plane are established. In the numerical model only half of the geometric model representing the workpiece can be thus taken into account. The respective boundary condition on the YZ symmetry plane, associated with determination of the symmetrical temperature field, is given by imposing the zero-heat flux  $\lambda \cdot \partial T / \partial n = 0$  in the direction normal to the symmetry plane.

In the computer simulation, the temperature field (Fig. 1), the temperature change rate, the microstructure transformation kinetics, the temperature-dependent material properties, and the latent heat released in phase transformations are computed at each time increment.

#### 3.2. Material properties

The material considered is 50CrV4 steel, with its chemical composition given in Table 1. The respective material properties, all considered in the simulation computations (Eqs. (1)–(2)) as temperature dependent, have been provided from different sources. Respective dependencies for the density (Fig. 2), specific heat (Fig. 3), and thermal conductivity (Fig. 4) are taken from [23], whereas the latent heat values tabulated in Table 2 are obtained respectively for the martensitic transformation from [28] and for ferrite and pearlite transformation from [29].

In the simulation, the temperature dependence of the heat transfer coefficient between the workpiece and surrounding air (Eq. (4)) is assumed, as proposed in [30]:

$$h = \begin{cases} 0.0668 \times T \left( \text{W}/(\text{m}^2 \text{ } ^\circ\text{C}) \right), & T_0 < T < 500 \text{ } ^\circ\text{C} \\ 0.231 \times T - 82.1 \left( \text{W}/(\text{m}^2 \text{ } ^\circ\text{C}) \right), & T \geq 500 \text{ } ^\circ\text{C} \end{cases} \quad (26)$$

#### 3.3. Laser characterisation

The performed computer simulations are run by considering the heat flux distribution  $q(x, y)$  of a 3-kW HPD laser used to conduct laser hardening experiments (Eq. (4)). The given laser beam has a  $23 \times 5$  mm interaction area with the workpiece whereas the parameters specifying the shape of the laser beam intensity distribution were evaluated based on the respective experimental validation of the laser beam intensity distribution, performed in [27]. Accordingly, the value  $m = n = 50$  is assumed in the computations performed herein with the heat flux distribution  $q(x, y)$  given by Eq. (23). In the computation of  $q(x, y)$ , the findings of [31,32] regarding dependence of the absorptivity of laser light by the workpiece's surface are taken into consideration. Accordingly, the absorptivity  $A$  is treated as a function of the interaction time and the laser beam power.

For the given laser characteristic and the laser located at its initial position, the normalised intensity of a laser beam distribution  $I(x, y)/I_0$  is displayed in the  $x > 0$  part of the laser beam interaction area in Fig. 5, while in the  $x < 0$  part the iso-curves  $R(x, y) = R_i$ ;  $R_i \in \{1 \cdot 10^{-4}, 1 \cdot 10^{-3}, 1 \cdot 10^{-2}, 1 \cdot 10^{-1}, 1\}$  are plotted. From the

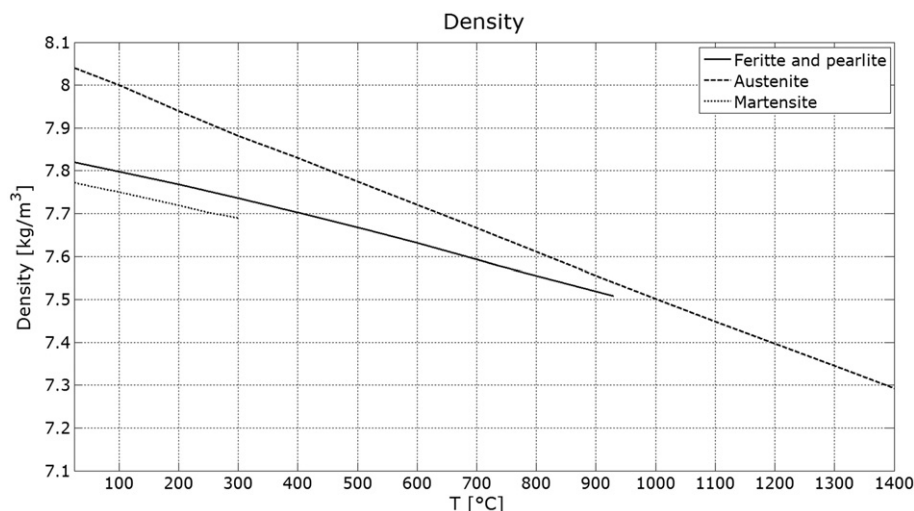


Fig. 2. Density of 50CrV4 steel from JmatPro 6.1 [23].

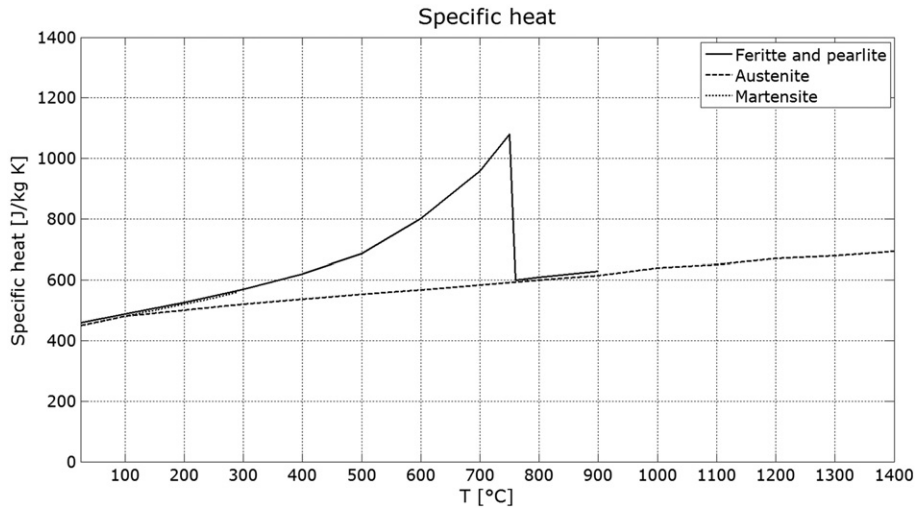


Fig. 3. Specific heat of 50CrV4 steel from JmatPro 6.1 [23].

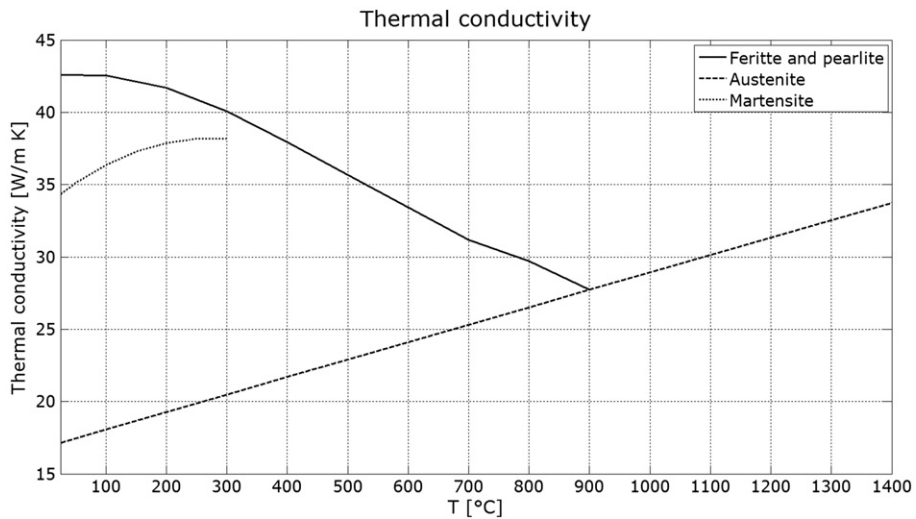


Fig. 4. Thermal conductivity of 50CrV4 steel from JmatPro 6.1 [23].

latter, all in Section 2.3 described properties of such a SG distribution are evident.

### 3.4. Simulation case studies

In the experimental part of this investigation, performed purposely to provide realistic data for physically trustful validation of the corresponding computer simulations, two sets of the process parameters, Case A and Case B, were considered (see Table 3). These two sets, which were chosen on an industrial experience basis, ensure a comparable maximum temperature on the surface of the workpiece despite different energy inputs.

To provide sufficient proof for adequacy of the presented approach to microstructure transformation kinetics during continuous heating

based on isothermal data and Scheil's additivity rule, the considered experiments are numerically treated in computer simulation by considering two approaches to material hardness determination. In the so-called 'rate dependent' computer simulation, the heating rate-dependent austenitisation temperatures  $Ac_1$  and  $Ac_3$  are considered in microstructure transformation kinetics, whereas in the so-called 'rate independent' computer simulation, the austenitisation temperatures  $Ac_1$  and  $Ac_3$  are assumed to be independent of the heating rate. The values of the austenitisation temperatures in the rate-dependent simulations are obtained from [23], while in the rate-independent simulations, they are obtained from [33], with a determination based on chemical composition of 50CrV4 steel (Table 1) as follows:

$$\begin{aligned}
 Ac_1 = & 723 - 7.08 \cdot Mn + 37.7 \cdot Si + 18.1 \cdot Cr + 44.2 \cdot Mo + 8.95 \cdot Ni \\
 & + 50.1 \cdot V + 21.7 \cdot Al + 3.18 \cdot W + 297 \cdot S - 830 \cdot N - 11.5 \cdot C \cdot Si \\
 & - 14 \cdot Mn \cdot Si - 3.1 \cdot Si \cdot Cr - 57.9 \cdot C \cdot Mo - 15.5 \cdot Mn \cdot Mo \\
 & - 5.28 \cdot C \cdot Ni - 6 \cdot Mn \cdot Ni + 6.77 \cdot Si \cdot Ni - 0.80 \cdot Cr \cdot Ni \\
 & - 27.4 \cdot C \cdot V + 30.8 \cdot Mo \cdot V - 0.84 \cdot Cr^2 - 3.46 \cdot Mo^2 \\
 & - 0.46 \cdot Ni^2 - 28 \cdot V^2 \text{ [}^\circ\text{C]}
 \end{aligned}
 \tag{27}$$

Table 2

Latent heat released during phase transformation.

Phase transformation	$\Delta H$ [J/m <sup>3</sup> ]
Ferrite → Austenite	$595 \cdot 10^6$
Pearlite → Austenite	$526 \cdot 10^6$
Austenite → Martensite	$640 \cdot 10^6$

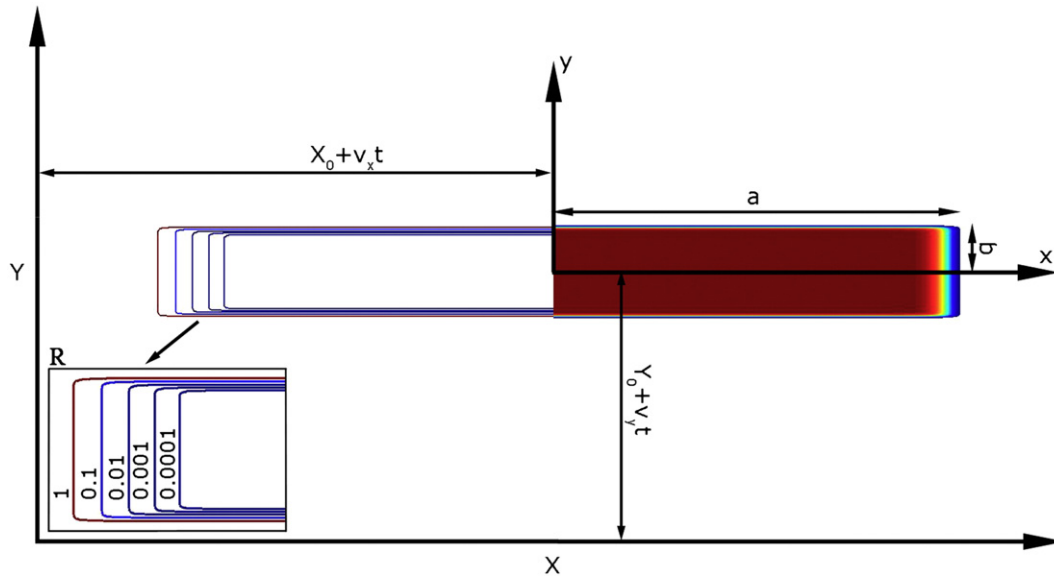


**Fig. 5.** Laser beam characterisation of a 3-kW diode laser with wavelength of 800–940 nm, focal length of 200 mm, and interaction area of 23 mm × 5 mm and  $m = n = 50$ .  $x < 0$ : Iso-curves  $R(x,y) = R_0$ ,  $x > 0$ : Normalised laser beam intensity distribution  $I(x,y)/I_0$ .

**Table 3**  
Characterisation of the initial material state and specification of the heat treatment parameters.

	Initial hardness	Initial microstructure	Preliminary treatment	$P$ [W]	$v_Y$ [mm/s]	$E_{int}$ [J/mm]	$q$ [W/mm <sup>2</sup> ]	$t_{tot}$ [s]
Case A	282HV <sub>0.5</sub>	$\alpha$ -Fe + P	Normalisation	1500	2	750	13	40
Case B	284HV <sub>0.5</sub>	$\alpha$ -Fe + P	Normalisation	2200	5	440	19	16

$$\begin{aligned}
 Ac_3 = & 912 - 370 \cdot C - 27.4 \cdot Mn + 27.3 \cdot Si - 6.35 \cdot Cr - 32.7 \cdot Ni \\
 & + 95.2 \cdot V + 190 \cdot Ti + 72 \cdot Al + 64.5 \cdot Nb + 5.57 \cdot W + 332 \cdot S \\
 & + 276 \cdot P + 485 \cdot N - 900 \cdot B + 16.2 \cdot C \cdot Mn + 32.3 \cdot C \cdot Si \\
 & + 15.4 \cdot C \cdot Cr + 48 \cdot C \cdot Ni + 4.32 \cdot Si \cdot Cr - 17.3 \cdot Si \cdot Mo \\
 & + 18.6 \cdot Si \cdot Ni + 4.8 \cdot Mn \cdot Ni + 40.5 \cdot Mo \cdot V + 174 \cdot C^2 \\
 & + 2.46 \cdot Mn^2 - 6.86 \cdot Si^2 + 0.322 \cdot Cr^2 + 9.9 \cdot Mo^2 \\
 & + 1.24 \cdot Ni^2 - 60.2 \cdot V^2 \text{ [}^\circ\text{C]} \quad (28)
 \end{aligned}$$

#### 4. Experimental investigation

The experimental work associated with the construction and validation of the herein presented numerical model of laser hardening is two-fold. On the one hand, considering experimentally the evolution of the temperature field determines the characteristics of laser energy input. Reliability of the obtained data, which represents the input data of the numerical model, is of essential significance for physical trustfulness of the simulation results. On the other hand, performing corresponding measurements of certain measurable quantities of interest, either partial or integral, such as the surface temperature field evolution and resulting hardness, validates adequacy of the numerical model used in the simulation. For the topic regarding laser energy characterisation, the reader is invited to read [27], where the related research is discussed. In this section, a description of the experiment is given, which is followed by a report of the corresponding measurement results.

##### 4.1. Laser hardening experiment

In the experiment, 100 × 100 × 15 mm cuboid samples made of 50CrV4 steel with the chemical composition tabulated in Table 1 were subject to laser hardening. The samples, which had been cut and milled to actual size from a 15.3 × 100.0 × 2000.0 mm rectangular cuboid, were

normalised in a furnace following the conventional procedure at a temperature of 875 °C [4]. As can be seen from the initial microstructure at 500× magnification displayed in Fig. 6, a fairly homogeneous distribution of ferrite and pearlite is obtained after normalisation. In Table 3, the respective average measured values of hardness are tabulated.

The sample size and the type of steel were selected based on the past experience with the heat treatment of hypo-eutectoid steels basis. The high hardenability of the used steel, simple geometric shape of the sample, and the suitable mass considering the energy input allow high heating and cooling rates, which in consequence enable a clear demonstration of the heating rate influence on the  $Ac_1$  and  $Ac_3$  temperature limits.

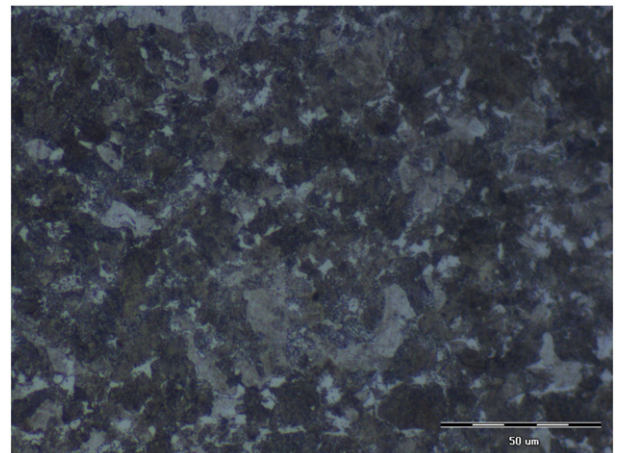


**Fig. 6.** Initial microstructure of normalised sample ( $\alpha$ -Fe + P microstructure) at 500× magnification.

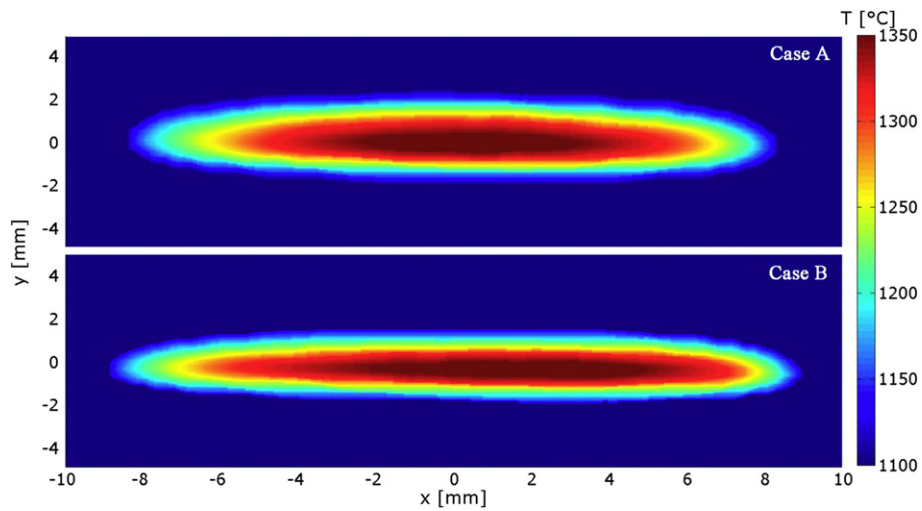


Fig. 7. Measured temperature field distribution (above 1100 °C) on the sample surface. Top panel: Case A at time of 30 s, Y = 60 mm. Bottom panel: Case B at time of 12 s, Y = 60 mm.

Prior to laser hardening, the samples were finely grinded to remove any contaminants from the surface. The experiment was conducted with the 3-kW HPD laser, whose detailed characterisation is given in Section 3.3. A surface area of the sample approximately 80 mm long and 23 mm wide and positioned in the middle of the sample symmetrically along the Y-axis was heat treated (Fig. 7). The heat treatment with the starting position of the laser beam 10 mm from the edge of the sample was performed by considering two different sets of process parameters referenced in Table 3 as Case A and Case B.

The specified process parameters selection, which is based on industrial experience, aims at attaining a comparable maximum temperature on the sample's surface. The process parameters, denoted in Table 3 by symbols  $P$ ,  $v_Y$ ,  $E_{int}$ ,  $q$ , and  $t_{tot}$ , are, respectively, the laser beam power, laser beam velocity along the Y direction, specific energy input per unit of length, constant heat flux affecting a  $23 \times 5$  mm large surface area of the sample beneath the moving laser source, and the total time of the laser travel.

#### 4.2. Surface temperature field measurements

During heat treatment the time evolution of the temperature distribution was measured on the sample surface exposed directly to the laser beam. For that purpose an E-MAqS thermal imaging camera mounted on the housing of the laser head and moving along with the laser beam was used together with the LompocPro software [34] for a corresponding analysis of the measured temperature field. The measurements were confined to the interval between 1000 °C and 1370 °C.

In Fig. 7 the respective surface temperature field distributions for Case A and Case B are displayed at the laser position  $Y = 60$  mm. The colour scale represents temperature distribution above 1100 °C, whereas a dark blue area is the area with temperatures below this limit. At this position the time evolution of the temperature distribution through the volume of the sample can be considered stabilised; the initial effects such as vicinity of the edge to the laser starting position ( $Y = 10$  mm) and uniform temperature distribution of the sample disappeared.

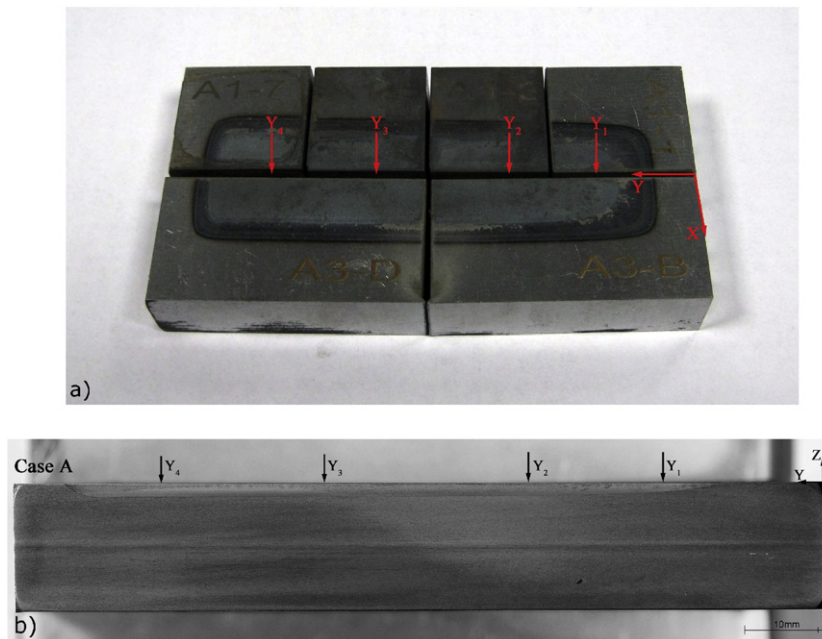


Fig. 8. Preparation of samples for hardness measurements with marked measurement positions: a) Water jet cut-up samples; b) cross-section in YZ symmetry plane subject to hardness measurement.

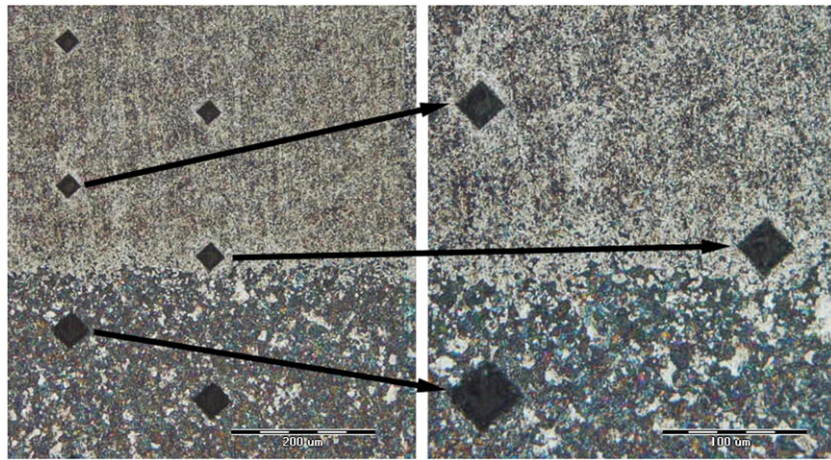


Fig. 9. Area of microstructure transition from martensite to the base material (Case A,  $Y = 60.0$  mm): Left:  $100\times$  magnification. Right:  $200\times$  magnification.

From the displayed temperature distributions in Fig. 7, the influence of applying different process parameters is mostly visible in the width of the observed temperature range. In Case B, which is the case with greater laser beam power and faster laser movement applied, the observed temperature range is narrower and longer than it is in Case A. On the other hand, the attained maximum temperatures are of the same magnitude (actually identical,  $1335\text{ }^{\circ}\text{C}$ ), as was intended when specifying the process parameters values for the two cases. Although the problem considered is supposed to be symmetrical with respect to the YZ plane, slight asymmetry with respect to the YZ symmetry plane (local y-axis) can be revealed from a detailed analysis of the displayed distributions. Possible reasons for that could be attributed to an inclination of the thermal imaging camera, vibration of the robot during the movement of the laser beam, and voltage fluctuations of the power supply at the input on the laser head.

#### 4.3. Through-thickness hardness measurements

After heat treatment, the samples were cut using a water jet, first along the YZ symmetry plane and subsequently each half into four pieces, as seen from the photograph in Fig. 8a. The obtained samples were then prepared in accordance with the ASTM E3-11 standard for further hardness measurements and microstructure analysis. The hardness was measured using a Zwick ZHU Z2.5 (HV0.5) hardness tester, whereas an Olympus GX 51 microscope was used in the microstructure analysis.

How the manifested time variation of the temperature field affects the phase transformations was investigated by measuring hardness through the sample thickness. In particular, the hardness was measured on the cross-section in the YZ symmetry plane with the measurements performed at distances of 18.5, 35.0, 60.0, and 80.0 mm from the edge of the sample in the Y-axis direction, and considering a stepping increment of 0.1 mm in the opposite direction of the Z-axis (Fig. 8b). Because of

later comparison with the corresponding computer simulation results aimed at improved correspondence evidence, the size of the measurement increment was chosen on the basis of the characteristic size of the FEs in the phase transformation domain (see FE mesh discretisation up to a depth of 2 mm in Fig. 15). The adequacy of the chosen increments is also proven indirectly by observing the microscope pictures of the microstructure in Fig. 9, where it is evident for the analysed Case A at the location  $Y = 60$  mm that the transition from a fully martensite microstructure into a partially transformed mixture of martensite with pearlite and ferrite is continuing into the base one, which takes place within the considered increment length (0.1 mm). This area is actually almost discrete.

The increased hardness that results from the formation of martensite microstructure was determined according to the results of the Jominy test obtained from [23], where all material points having hardness above 550 HV have been included in the domain of increased hardness. For Case A and Case B, the respective depths of increased hardness  $Z_{\max\_m}$  obtained by hardness measurement are tabulated in Table 4, and corresponding hardness values are displayed graphically in Fig. 10. The area of increased hardness as well as the difference between stabilised ( $Y = 35, 60, 80$  mm) and edge-affected ( $Y = 18.5$  mm) hardness distribution is clearly expressed in the displayed graphs.

#### 5. Simulation results and their validation

The great potential of solving field domain problems numerically is its capability of providing information about the physical state at any point of the considered domain, thus enabling to get a better insight and strengthening our understanding of the phenomena under consideration. Being aware of the limited potential of any experimental investigation, the importance of that is expressed further when treating problems for which the respective field distributions are subject to time variation. For example, for the considered laser hardening process, time variation

Table 4  
Measured and computed maximum depths of increased hardness with respective deviations.

Values in mm	Case A					Case B						
	$Z_{\max\_m}$	Experiment		Computer simulation			$Z_{\max\_m}$	Experiment		Computer simulation		
		$Z_{\max\_c}$	$\Delta Z_{\max\_d}$	Rate dependent		$Z_{\max\_c}$		$\Delta Z_{\max\_d}$	$Z_{\max\_c}$	$\Delta Z_{\max\_d}$	Rate independent	
				$Z_{\max\_c}$	$\Delta Z_{\max\_d}$						$Z_{\max\_c}$	$\Delta Z_{\max\_d}$
18.5	1.0	1.1	+0.1	1.3	+0.3	1.0	1.0	0.0	1.1	+0.1		
35.0	1.5	1.5	0.0	1.7	+0.2	1.1	1.1	0.0	1.3	+0.2		
60.0	1.5	1.5	0.0	1.8	+0.3	1.1	1.1	0.0	1.3	+0.2		
80.0	1.5	1.6	+0.1	1.8	+0.3	1.1	1.1	0.0	1.3	+0.2		

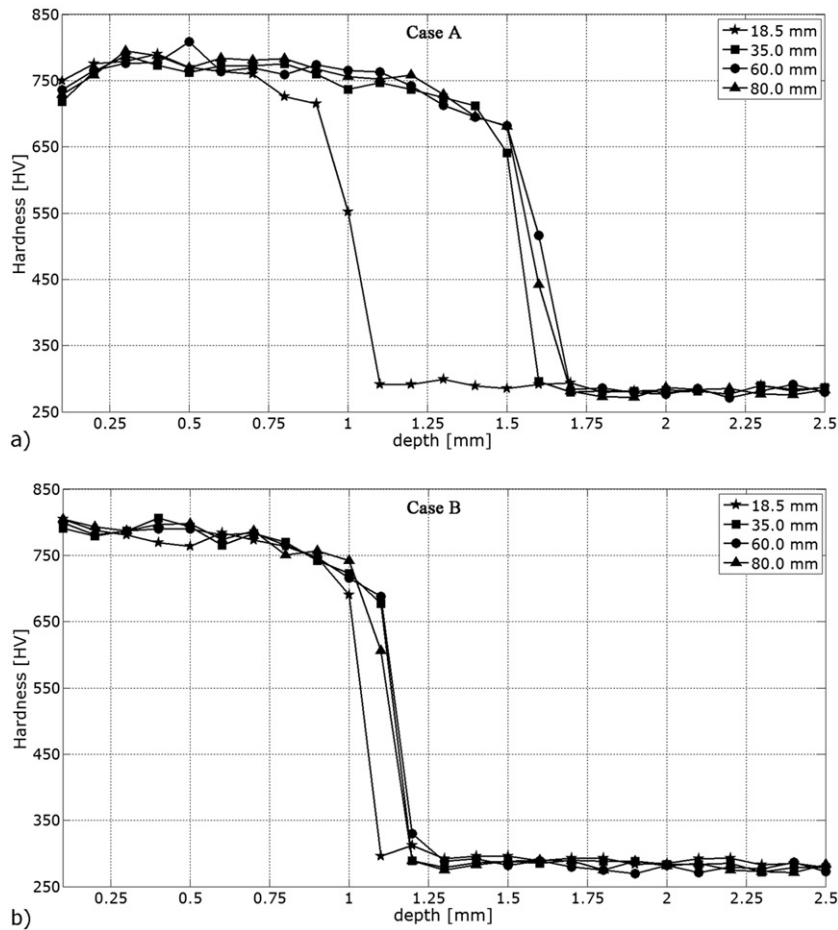


Fig. 10. Measured hardness values v. depth at  $Y = [18.5, 35.0, 60.0, 80.0]$  mm on the YZ symmetry plane: a) Case A; b) Case B.

of the temperature at one point is of utmost interest because it determines the kinetics of phase growth and final microstructure.

The developed numerical model can be considered useful for common engineering practice, either in process analysis or in its design, only if its physical trustfulness is proven. In this regard, the model has to pass a series of severe numerical and physical validation tests, thus demonstrating its susceptibility to variation in the input data and ability to reproduce complex physical behaviour in a realistic way. Herein, we assume that purely numerical issues concerning adequate domain discretisation, time increments, and appropriate choice of the FE type required to obtain numerically accurate and robust solutions are satisfactorily tackled. The remaining task is to submit the numerical model to a variety of significantly different input data and to confront the computed simulation results with the experimentally obtained ones. This essential task is demanding as it requires adequate experimentation and corresponding measurements.

For the purpose of validation, computer simulations of the heat treatment process considering Case A and Case B's technological parameters were run. In the subsequent two sections, the respective simulation results are correspondingly validated with respect to the measurements presented in Section 4.

### 5.1. Validation of the temperature field evolution

The respective computed surface temperature field distributions at the laser's position ( $Y = 60$  mm), considering values above  $1100$  °C, are displayed in Fig. 11, top panel. Taking advantage of the symmetry with respect to the Y-axis, the Case A distribution is displayed on the

left side ( $x < 0$ ) while the Case B distribution is displayed on the right side ( $x > 0$ ) of the figure.

The computed temperature distributions are now compared to the measured ones, displayed in Fig. 7. First, because of the evidenced slight asymmetry in the measured temperature distributions, these distributions are symmetrised to simplify the comparison. The resulting difference between the measured and computed temperature fields is graphically displayed in Fig. 11, bottom panel. The range of respective temperature differences for both cases is given by the interval  $[-50, +50]$  °C, with the average difference evaluated in the temperature field area above  $1100$  °C being  $+2$  °C and  $-10$  °C, respectively. The established discrepancy between the compared temperature distributions with respect to the temperature of  $1100$  °C is thus limited to  $[-3, +4]$  % for Case A and  $[-4, +4]$  % for Case B.

As can be concluded by observation of the displayed distributions in Fig. 12, the highest discrepancy appears in the area behind the laser beam. Considering rapid changing of the temperature field in this area (Fig. 11), this evidence may be justified by the thermal camera characteristic. Capturing of the temperature field is limited by the size of a pixel and by the number of frames per second. The thermal camera resolution is approximately 4 pixels per millimetre, and the camera can record 7 frames per second. The computed temperature distributions in Fig. 11 demonstrate a rapid and great temperature decrease manifested over the length of a few pixels, which is in turn reflected in less accurate measuring results in this area. As in Case B, due to higher velocity of the laser beam, the same temperature decrease is established within a narrower area than in Case A; the respective discrepancy between the computed and measured temperature distributions is greater than in Case A. Nevertheless, in

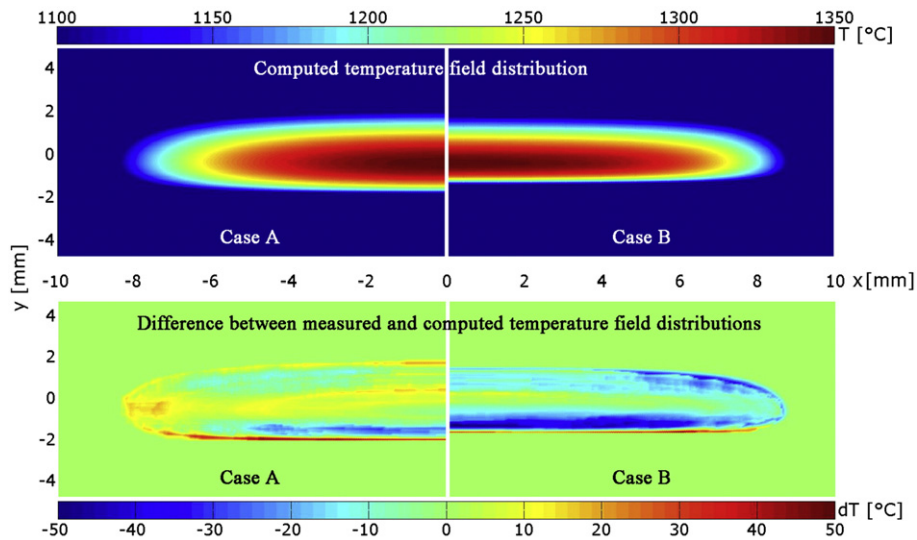


Fig. 11. Computed temperature validation (above 1100 °C) on the sample surface.  $x < 0$ : Case A at time 30 s,  $Y = 60$  mm;  $x > 0$ : Case B at time 12 s,  $Y = 60$  mm.

both cases the maximal discrepancy does not exceed  $\pm 4\%$  with respect to the temperature level of 1100 °C.

### 5.2. Validation of the material hardness evaluation

Following the material hardness determination presented in Section 2.2.3, hardness can be evaluated at any material point subject to temperature variation. Consider first the results obtained by considering heating rate-dependent austenitisation temperatures  $Ac_1$  and  $Ac_3$  in microstructure transformation kinetics (i.e., the rate-dependent simulation). In Fig. 14, the calculated hardness through the thickness at the cross-section  $Y = 60$  mm is compared to the measured one (see Fig. 10) for Case A and Case B. With no hesitation, it can be concluded that despite significant diversity in the applied process parameters, very good agreement between the computed and measured results is demonstrated in both cases. This proves the physical objectivity of the entire numerical model, which gives the model the necessary credibility for its potential use in industrial practice.

But it must be emphasised that crucial to this demonstrated physical objectivity is the adopted mathematical model for kinetics of phase growth and the appropriateness of the proposed approach applied in its numerical implementation. For the material hardness resulting after laser heat treatment, the conditions during heating are decisive because formation of austenite depends essentially on the actual heating

rates and maximum attained temperature. The impact of different process parameters applied in Case A and Case B is clearly demonstrated in Fig. 14 by the established depth of increased hardness, which is in Case A greater than in Case B. The estimated sizes are, respectively, 1.5 mm and 1.1 mm.

Further understanding of the resulting hardness through the thickness of the sample, as a function of the applied process parameters, can be gained by observing the evolution of the phase transformation for a particular material point. In this discussion we focus, for better comparison and understanding of the impact of applying different process parameters, on the same material point in both cases. Because the point where the difference in physical behaviour and causality between the related phenomena is so specific and explicit, we consider the point positioned 1.1 mm under the heat-affected surface at the cross-section to be  $Y = 60$  mm. The plotted temperature and temperature change rate evolutions in Fig. 12, which give rise to the phase transformation evolutions displayed in Fig. 13, clearly reveal the physical basis for the established hardness difference after cooling at this point (see Fig. 14).

As shown in Fig. 12, although the maximum temperature in Case A is higher in comparison to Case B at depth 1.1 mm, the opposite is true for the corresponding temperature changes. Actually, in analysis of the plotted evolutions, not much effort is required to identify separate effects of the laser beam power and laser beam velocity on the temperature and temperature change rate evolutions. The established

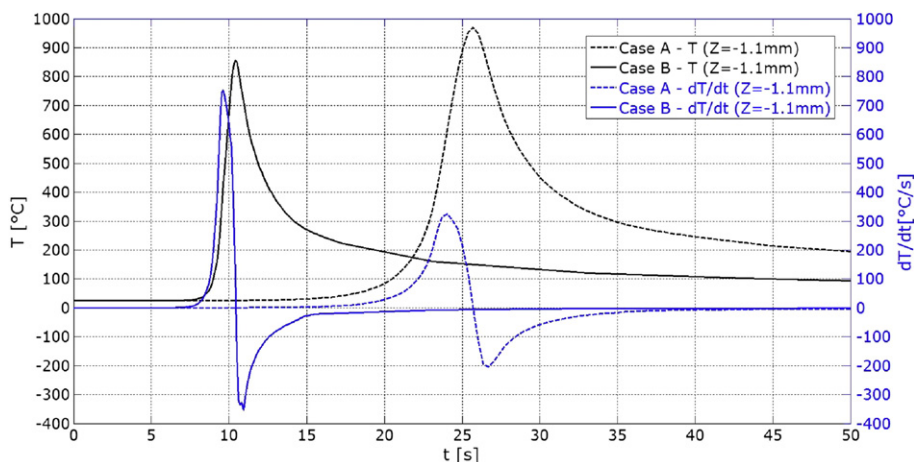


Fig. 12. Case A and Case B's respective temperature and temperature change rate evolutions at the cross-section  $Y = 60$  mm and  $Z = -1.1$  mm.

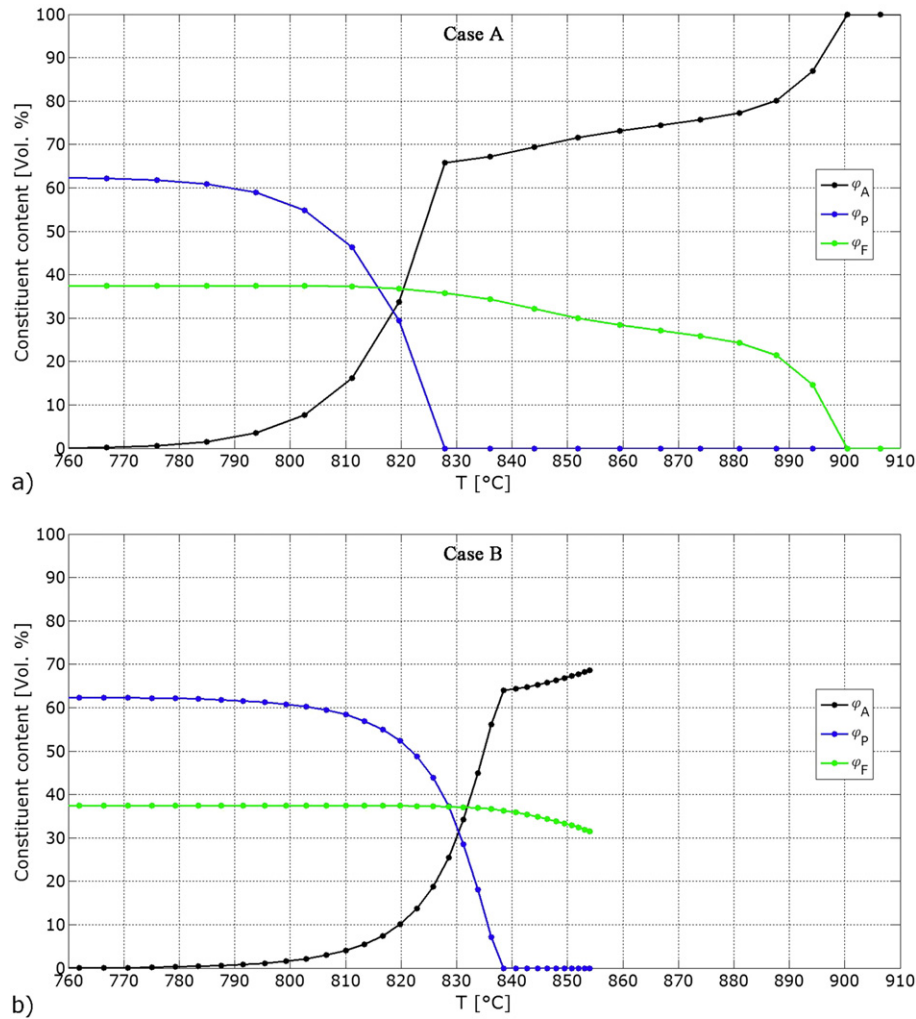


Fig. 13. Evolution of phase transformation at the cross-section  $Y = 60 \text{ mm}$ ,  $Z = -1.1 \text{ mm}$ . a) Case A: Complete austenitisation; b) Case B: Partial austenitisation.

difference in maximum temperatures, 970 °C in Case A and 855 °C in Case B, is a direct consequence of different heat inputs resulting at that point due to the difference in the applied process parameters (see Table 3). From the displayed evolutions in Fig. 13, providing the respective volume fractions of emerging austenite ( $\varphi_A$ ) and disappearing pearlite ( $\varphi_P$ ) and ferrite ( $\varphi_F$ ) dependent on temperature, it can be concluded that while in Case A complete austenitisation has occurred in the transformation, in Case B, the transformation is partial due to different heating conditions (i.e., lower maximum temperature and higher temperature change rate, see Fig. 12) as a consequence of greater laser beam power and laser beam velocity. Furthermore, the higher temperature change rate affects the initial temperature for austenite formation  $T_{A_5}$ , which indicates the formation of 1% of austenite from pearlite. From the simulation,  $T_{A_5}$  is 780 °C in Case A and 795 °C in Case B. The evidenced shift from 820 °C in Case A to 830 °C in Case B of the start of ferrite transformation into austenite can also be attributed to the higher temperature change rate established in Case B.

All characteristic phase transformation histories to which individual material points at different depths were subjected are revealed from the course of the curves representing computed hardness distribution in Fig. 14. Namely, the resulting hardness at the point is a function of the microstructure resulting at the end of the heating phase and the maximum temperature attained. With regard to the latter, four distinct temperature areas, T-1, T-2, T-3, and T-4 (see Section 2.2.3), each having a specific impact on the hardness, were specified. In the hardness distributions in Fig. 13, this impact is clearly manifested. In this regard five

characteristic depth zones of hardness, denoted as a, b, c, d, and e, can be identified through the thickness. Evidently, there is a simple correlation between the temperature areas T-1, T-2, T-3, and T-4 and depth zones of hardness a, b, c, d, and e.

Zone a, which includes points with respective temperature evolutions belonging to the temperature area T-1, is a zone with no phase transformation during heat treatment. The corresponding material hardness is identical to the average measured hardness before laser heat treatment, which is 282 HV for Case A and 284 HV for Case B.

Zone b, which includes points with respective temperature evolutions belonging to the temperature area T-2, reflects hardness caused only by transformation from pearlite to austenite during heating (see Fig. 14a) and subsequent transformation from the formed austenite to martensite during cooling. The resulting hardness is determined by Eq. (15), considering hardness of constituents in the phase mixture. At the expense of pearlite transformed to austenite, high-carbon martensite is mainly in zone b, but some retained austenite is also obtained after hardening. In general, zone b is characterised by a rapid, almost discreet jump in hardness due to heating the material above  $A_{c1}$ .

Zone c, which includes points with respective temperature evolutions belonging to the temperature area T-3, has pearlite transformed while ferrite becomes austenite with low carbon content during heating (see Fig. 13b). However, depending on maximum temperature and temperature change rate, different degrees of inhomogeneous austenite can occur. The resulting hardness in zone c is also determined by Eq. (15), considering hardness of constituents in the phase mixture,

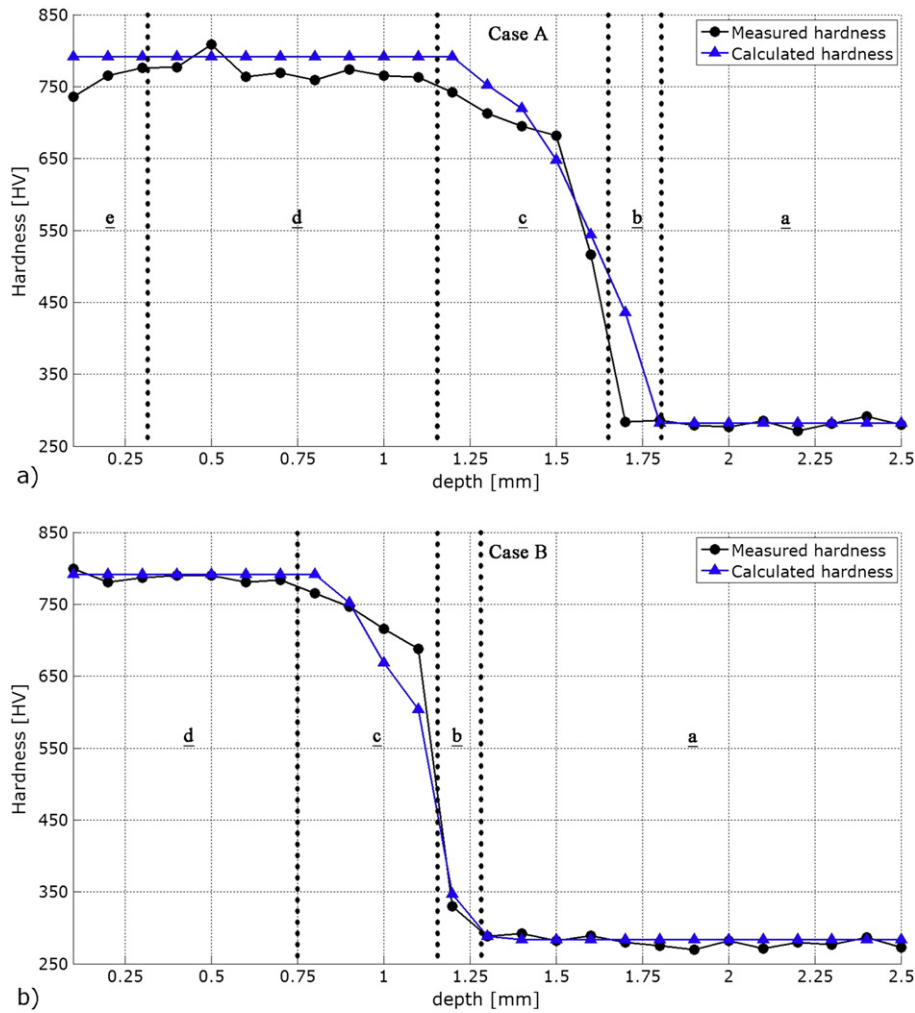


Fig. 14. Calculated and measured hardness values v. depth at  $Y = 60$  mm on the YZ symmetry plane: a) Case A; b) Case B.

where only some ferrite transformed into austenite affects calculated hardness.

Zone d, which includes points with respective temperature evolutions belonging to the temperature area T-4, contains (due to homogenisation of austenite during heating) almost fully homogenised martensite with a small amount of retained austenite formed after cooling. Corresponding hardness of homogenised martensite is constant and around 792 HV.

Always belonging to the temperature area T-4 are material points exhibiting increased grain growth of austenite as a consequence of rapid heating and high austenitisation temperatures, such as in domains very close to the laser source. After cooling, a slight decrease in martensite hardness of such increased austenite grain size can happen. In Fig. 14, this effect can be observed in hardness measurement in zone e for Case A, whereas the same effect is not evident in Case B. The respective boundary between the zones d and e is thus defined based on the exhibited decrease in hardness as a consequence of austenite grain growth at higher temperatures.

Considering very good agreement achieved between the computed and measured results in the rate-dependent simulation (Fig. 14), a question arises as to the effect of microstructure transformation kinetics with austenitisation temperatures  $Ac_1$  and  $Ac_3$  assumed to be independent of the heating rate. A comparative analysis of the obtained computer simulation results is now based on the computed maximum depths of increased hardness  $Z_{\max\_c}$  resulting from the formation of martensite microstructure, which are compared in Table 4 against the corresponding measured values  $Z_{\max\_m}$ . In the table, respective deviations  $\Delta Z_{\max\_d}$

of the calculated values from the corresponding measurements are tabulated.

$$\Delta Z_{\max\_d} = Z_{\max\_c} - Z_{\max\_m}. \quad (29)$$

Upon considering the tabulated values, it follows (as expected) that the computed values are closer to the measured values when the computer simulation is rate dependent with respect to the determination of the austenitisation temperatures  $Ac_1$  and  $Ac_3$ . The accordance between the computation in the case of rate-dependent simulation and measurement is even more pronounced when comparing the respective finite element representation of the martensite area in the  $58.2 \text{ mm} \leq Y \leq 61.8 \text{ mm}$ ,  $0.0 \text{ mm} \leq Z \leq -3.6 \text{ mm}$  domain of the symmetry plane with the microscope picture of the microstructure in Fig. 15.

## 6. Conclusions

In this paper, heat transfer and microstructure evolution (the physical phenomenology of the laser hardening process) were successfully transferred to the virtual environment. The numerical model used in a computer simulation of the process was experimentally validated by measuring the temperature on the surface of the workpiece and by hardness measurement at different locations and depths on the workpiece cross-section for two different energy inputs. A good match between the measured and calculated temperatures on the surface of the workpiece proves adequacy of the applied thermal boundary

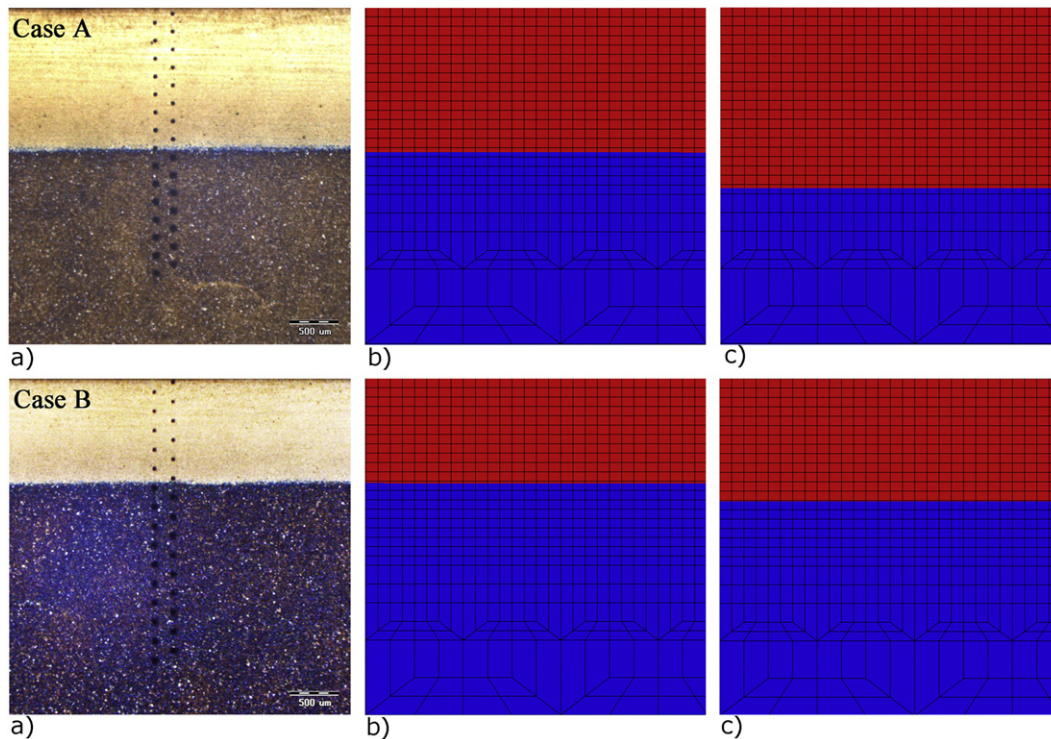


**Fig. 15.** Comparison of martensite area in the real sample and as determined by computer simulation. a) Experiment; b) rate-dependent simulation; c) rate-independent simulation. Top panel: Case A. Bottom panel: Case B.

conditions—in particular, those associated with the laser beam energy distribution. Good agreement achieved between corresponding measured and calculated hardness in case of rate-dependent simulations indicates a sufficiently good mathematical model for the calculation of phase transformations induced by rapid heating.

According to rate-dependent simulation, the computed depth of increased hardness deviates from the experimentally determined one in Case A by a maximum of +0.1 mm while in Case B there is no deviation. On the contrary, when simulation is considered to be rate independent, the considered maximal deviations are, respectively, +0.3 mm and +0.2 mm. A better match in case of rate-dependent simulations indicates that during the laser hardening process, microstructural kinetics, as presented in chapter 2.2.1, must be considered.

Furthermore, results of simulations also show that different laser input energies have a significant impact on the kinetics of austenite formation (when transformation from pearlite to austenite begins and when transformation from ferrite to austenite begins). In terms of the material point under the heat-affected surface, the austenitisation temperature is higher when experiencing a higher temperature change rate, as in Case B. In comparison to Case A, the corresponding start of austenite formation in Case B was actually found to be 15 °C higher and the start of transformation from ferrite to austenite was 10 °C higher.

It is also important to emphasise, that in view of appropriate process design the corresponding temperature on the workpiece surface should always be simultaneously considered in connection to the laser beam power and to the laser beam velocity or interaction time of laser beam with material points on the workpiece surface. Furthermore, essential technological parameters for laser hardening are in some cases laser nominal power and velocity of laser beam, or alternatively controlled temperature on surface and laser beam velocity. In considered cases A and B the input parameters were laser beam power and laser beam velocity. In many applications in industrial environment there are, however, cases where the laser operator can set the laser beam velocity and surface temperature on the workpiece, which is controlled by a thermal camera and correspondingly adjusted by automatic changing of the

laser beam power. This kind of technological solutions is usually provided for safety reasons in case of complex workpiece geometry. In industrial cases, where surface of workpieces is in common diverse and laser hardening is applied in 3D space, applying initial constant power through the entire process could damage the surface of workpiece due to different heat conditions established during laser hardening operation. In these cases, in order to protect the workpiece surface against melting, laser beam power is variable while laser beam velocity and controlled temperature on surface are specified input parameters. Thus, in order to ensure specified hardness profile by maintaining the prescribed controlled temperature on the workpiece surface, the laser technician should take into consideration, when specifying laser beam velocity, the correlation between laser beam velocity and the depth of increased hardness.

As shown from the analysed cases, the same maximum temperature attained on the surface at  $Y = 60$  mm is not enough to determine the depth of increased hardness. From the performed experiments, it is evident that change in the velocity of the laser beam from 2 mm/s to 5 mm/s decreases the depth of increased hardness from 1.5 mm to 1.1 mm, which has a great impact on the workpiece's final state.

#### Acknowledgement

The first author appreciates the partial financial support of the European Union's European Social Fund Operation implemented in the framework of the Operational Programme for Human Resources Development (P-MR-10/86) for the period 2007–2013.

#### References

- [1] J. Grum, in: C.H. Gür, J. Pan (Eds.), *Handbook of Thermal Process Modeling of Steels*, Taylor & Francis Group, Florida, 2009, pp. 499–626.
- [2] M.F. Ashby, K.E. Easterling, *Acta Metall.* 32 (1984) 1935–1948.
- [3] W.B. Li, K.E. Easterling, M.F. Ashby, *Acta Metall.* 34 (1986) 1533–1543.
- [4] A.S.M. International Handbook Committee, *ASM Handbook Volume 04 – Heat Treating*, ASM International, 1991.

- [5] C. Şimşir, Doctoral Thesis, Middle East Technical University, February (2008).
- [6] J. Orlich, H. J. Pietrzeniuk, Atlas zur Wärmebehandlung der Stähle, M.B.H. Verlag Stahleisen, Düsseldorf, Band 4, 1976.
- [7] D. Deng, Mater. Des. 30 (2009) 359–366.
- [8] V. Colombo, A. Mentrelli, T. Trombetti, Eur. Phys. J. D 27 (2003) 239–246.
- [9] M.K.H. Leung, H.C. Man, J.K. Yu, Int. J. Heat Mass Transf. 50 (2007) 4600–4606.
- [10] S. Skvarenina, Y.C. Shin, Surf. Coat. Technol. 201 (2006) 2256–2269.
- [11] N.S. Bailey, W. Tan, Y.C. Shin, Surf. Coat. Technol. 203 (2009) 2003–2012.
- [12] D. Farias, S. Denis, A. Simon, Key Eng. Mater. 46–47 (1990) 139–152.
- [13] S. Denis, D. Farias, A. Simon, in: L. Karlsson, L.-E. Lindgren, M. Jonsson (Eds.), Mechanical Effects of Welding, Springer Berlin Heidelberg, 1992, pp. 57–65.
- [14] W.A. Johnson, R.F. Mehl, Trans. AIME 135 (1939) 416–458.
- [15] M. Avrami, J. Chem. Phys. 7 (1939) 1103–1112.
- [16] T. Mioković, V. Schulze, O. Vöhringer, D. Löhe, Mater. Sci. Eng. A 435–436 (2006) 547–555.
- [17] SIMULIA, ABAQUS/Standard 6.12 Analysis User's Manual, 2012.
- [18] M. Yaakoubi, M. Kchaou, F. Dammak, Comput. Mater. Sci. 68 (2013) 297–306.
- [19] L. Orazi, A. Fortunato, G. Cuccolini, G. Tani, Appl. Surf. Sci. 256 (2010) 1913–1919.
- [20] H.J.M. Geijselaers, Doctoral Thesis, University of Twente, October (2003).
- [21] E. Scheil, Anlaufzeit der Austenitumwandlung, Arch. Eisenhüttenwes., 121935, 564–567.
- [22] R.C. Sharma, Principles of Heat Treatment of Steels, New Age International (P) Ltd., New Delhi, 1996.
- [23] Sente Software Ltd, JMatPro 6.1 User's Manual, 2011.
- [24] C. Li, Y. Wang, Z. Zhang, B. Han, T. Han, Opt. Lasers Eng. 48 (2010) 1224–1230.
- [25] P. De la Cruz, M. Odén, T. Ericsson, Int. J. Fatigue 20 (1998) 389–398.
- [26] R. Menzel, Photonics Linear and Nonlinear Interactions of Laser Light and Matter, Second ed. Springer, Berlin, 2007.
- [27] M. Bojinović, N. Mole, U. Artiček, B. Štok, 9th International Conference on Industrial Tools and Material Processing Technologies ICIT & IPT, 9–11 April, Ljubljana, 2014, pp. 237–242.
- [28] S.-J. Lee, Y.-K. Lee, Scr. Mater. 60 (2009) 1016–1019.
- [29] S.H. Kang, Y.T. Im, J. Mater. Process. Technol. 192–193 (2007) 381–390.
- [30] C. Li, Y. Wang, H. Zhan, T. Han, B. Han, W. Zhao, Mater. Des. 31 (2010) 3366–3373.
- [31] H. Pantsar, V. Kujanpaa, J. Laser Appl. 16 (2004) 147–214.
- [32] H. Pantsar, V. Kujanpaa, Surf. Coat. Technol. 200 (2006) 2627–2633.
- [33] O.G. Kasatkin, B.B. Vinokur, V.L. Pilyushenko, Met. Sci. Heat Treat. 26 (1984) 27–31.
- [34] Fraunhofer IWS Dresden, LompocPro 7.6 User's Manual, 2010.